Nanostructured Pd—Cu Catalysts Supported on Zr—Al and Zr—Ti for Synthesis of Vinyl Acetate

Alberth Renne Gonzalez Caranton,[a] Jean Dille,[b] Jade Barreto,[c] Fernando Stavale,[c] José Carlos Pinto,[a] and Martin Schmal*[a]

Renewable ethylene can be obtained by dehydration of bio-ethanol and used for production of vinyl acetate (VAM) through reaction with acetic acid (AcOH), using Pd—Cu catalysts. In the present manuscript, structural characterizations of Pd—Cu/ZrO_2 catalysts show that these systems present cubic structure with different spatial distributions. Particularly, it is shown that combustion of ethylene and acetic acid can be inhibited below 180 °C, maximizing the rates of VAM formation, when the catalysts are modified with Ti^{+4}. The effects of AcOH concentration on rates of VAM formation show that higher AcOH concentrations favor the formation of undesired byproducts, while lower AcOH concentrations favor effects related to O_2 mobility, which can lead to surface decomposition. VAM formation is favored, with selectivities ranging from 0.8 to 1.0. XPS results indicate the existence of metallic Pd, CuO species and Zr species, in agreement with IR results. DRIFTS results also show that different Pd-acetate intermediates can be present, depending on the electronic effects associated to Pd—Cu and Zr species.

Introduction

The annual production of acetic acid, acetic anhydride, acetaldehyde and vinyl acetate monomer (VAM) is of the order of 6×10^9 kg/year only in the United States; however, the production of VAM consumes about 65% of the worldwide production of acetic acid.[1] VAM is a flammable, volatile and colorless liquid, with boiling point between 72–73 °C, used mostly for manufacture of poly(vinyl acetate) (PVAc) and PVAc derivatives, including poly(vinyl alcohol) (PVOH) and poly(ethylene-co-vinyl alcohol) (EVA).[2,3] Several studies have shown that Pd—Au alloys promote the catalytic coupling between acetic acid and ethylene with surface oxygen, reducing the probability of direct combustion of adsorbed species and leading to production of VAM.[4–6] This chemical route is useful for manufacture of VAM, presenting structure sensitivity for ethylene acetoxidation, normally attributed to the ensemble architecture provided by Pd—Au alloys.[7,8] However, commercial

SiO$_2$ supports do not possess the necessary alkalinity to maintain the stability of Pd—Au alloys. For this reason, it is usually necessary to add a cation (such as potassium, through KOAc) to promote electron transfer from the alkali to the metal and enhance the adsorption capacity.[9] Despite the development of Pd—Au/K-SiO$_2$ catalysts, it is still difficult to understand why sintering of Pd particles takes place at real operation conditions. Lercher et al[10] claimed that K^{+2} promotes the dynamic self-organization of Pd—Au alloys during the formation of intermediate species related to ethylene dissociation of C—C and C—H chemisorbed intermediates, formation of monodentate and bidentate acetate species related to acetic acid chemisorption over PdAu ensembles and desorption of VAM from Pd—Au active sites. [10]

The nature of copper species over ZrO$_2$ has been the subject of extensive researches. Copper oxide species play important roles in the catalytic activity of many processes, including CO$_2$ hydrogenation and selective oxidation.[11,12] The phase stabilization of ZrO$_2$ allows for enhancement of the oxygen mobility, depending on the activation conditions and affecting the particle sizes, redox properties and final catalyst reactivity.[13,14] Alternative catalyst preparation strategies can be based on the preparation of mixed materials by adding oxides, such as Al$_2$O$_3$ and TiO$_2$ into the ZrO$_2$ matrix, which can provide important complementary properties, including the appropriate acid/base balance, textural properties, thermal stability, among others.[15,16]

Copper/palladium bimetallic alloys present cubic arrangement, synergies and interactions that can be attributed to the particular electronic configurations and morphological effects of these bimetallic alloys, which can also lead to surface energy variations.[17,18] Particularly, the use of sonochemistry can provide catalysts with different morphologies, including nanotubes, nanodendrimers and nanorods, which can be subject to

[a] A. R. Gonzalez Caranton, Prof. J. C. Pinto, Prof. M. Schmal
Departament of Chemical Engineering (COPPE)
Federal University of Rio de Janeiro
128 Centro de Tecnologia Bl. G,
Rio de Janeiro 29141-972 (Brazil)
E-mail: schmal@peq.coppe.ufrj.br

[b] J. Dille
Departament of Metallurgircal and Materials Engineering
Federal University of Rio de Janeiro
Centro de Tecnologia, Bloco F
Av. Horácio Macedo, 2030
Cidade Universitária
Rio de Janeiro 21941-598 (Brazil)

[c] J. Barreto, F. Stavale
Brazilian Center for Research in Physics
Ministry of Science, Technology,
Innovation and Communication of Brazil
Rua Xavier Sigaud 150
Urca 22290-180 (Brazil)

distinct quantum effects.[19,20] For instance, Gao and Wayne[8] studied the VAM reaction with Pd−Au catalysts and concluded that Pd−Au alloys were more active than the bimetallic Pd−Au materials due to segregation effects. The Pd−Cu catalysts were also used to perform acetoxidation reactions in homogeneous media,[21] indicating that the active metal is reduced during the reaction with ethylene, which is then converted to VAM and acetaldehyde.[22] Therefore, copper can influence the reaction mechanism significantly, when compared to the transition metal catalysts.[23]

Bimetallic alloys have received significant attention in the literature due to their superior properties, when compared to the respective monometallic systems,[24] allowing for improvement of the surface properties, shape and reactivity of the catalyst and composition of product streams.[25,26] Theoretically, the highest atomic efficiencies can be achieved when the size of the metal particle is similar to the size of single atoms;[27] however, with the decreasing particle size, aggregation effects usually become important.[27,28] The isolation of one of the metals by the second metal improves the interfacial properties, due to synergetic effects between the two metals, associated with ensemble and electronic (ligand) effects.[29] For instance, alloying of a second metal with Pd can reduce the ensemble, leading to reduction of multi-bonded ethylene species.[30] It has been reported that Pd atoms can be isolated easily to form single atoms with Cu, leading to excellent selectivity towards hydrogenation and dehydrogenation reactions.[31,32] In comparison with Pd−Au alloys, where small changes occur in the atomic distance, isolated Pd species can lead to dramatic changes of the TOF values.[4] Additionally, in Pd−Cu alloys the charge transfer between the d-states of Pd and adsorbed O species can cause the increase of O binding on Cu sites and lattice bonds of Pd−Cu,[33] which are important for vinyl acetate formation.[66] In agreement with the literature, it shows the downshift of the d band center of Pd which forms different arrangements along the [111] lattice of an fcc cell unit, influencing the catalytic activity.[34] Then copper acts as a promoter, improving the stability of a second metal; the CuO reduction facilitates the H_2 spillover and affects the reduction[35] and exposition of a second metal, also exhibiting the excellent redox properties provided by the copper nanoclusters.[25,36] Otherwise, copper clusters form bimetallic hetero-structures with Pd, due to the donor capacity of electrons, as $PdCu_x$ species remain stable over the copper clusters during the reaction.[37]

Based on the previous remarks, the main objective of the present work is to study the catalytic performance of Pd−Cu cubic nanostructures, supported on modified ZrO_2-Al^{+3} and ZrO_2-Ti^{+4}, for production of vinyl acetate monomer, in the temperature range between 150 and 200 °C at atmospheric pressure. The present work investigates the properties and structures of the analyzed catalysts and investigates the reactivity, formation of intermediates on cubic species and the effects on Pd acetate intermediates formed in situ over Pd−Cu species at the analyzed reaction conditions.

Results and Discussion

Crystal Structure and Composition of ZrO_2-Based Catalysts Containing Pd and Cu

The ZrO_2 sample exhibited low crystallinity and was apparently amorphous. The crystallite structure of the catalyst was determined with help of the Rietveld refinement method. The obtained results and respective cell parameters are presented in Figure 1 and Table 1.
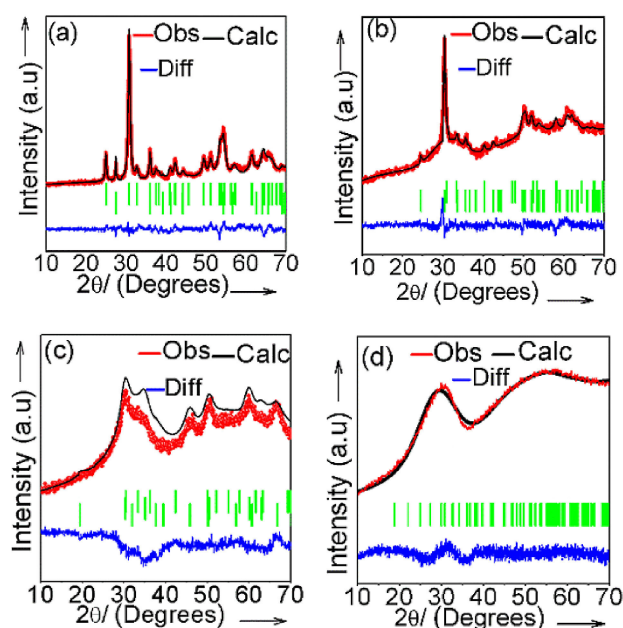

Figure 1. XRD Rietveld patterns: (a) CZT, (b) PCZT, (c) CZA and (d) PCZA. The black curves represent the experimental diffraction patterns, while the red lines represent the calculated patterns. The blue curves show the difference between calculated and experimental data. The green lines correspond to Bragg positions.

Table 1. Refined crystal structure parameters and reliability factors for ZrO_2-based catalysts.

Cell parameter	CZA	CZT	PCZA	PCZT
a	3.705	4.590	4.815	3.906
b	3.705	4.590	5.511	3.906
c	4.621	2.966	6.062	4.458
O1 Occ Ph1	1.341	0.1948	0.00	0.875
O1 Occ Ph2	0.01	4.907	0.00	1.098
R_W	5.56	12.24	1.40	8.60

The XRD patterns for the PCZA sample indicate materials of low crystallinity, caused by the deformations that result from curvature effects and produce microstrains, due to the hygroscopic nature of the materials. The background used for Rietveld refinement was modeled as a polynomial function, to describe the anisotropic crystallinity and reduce the differences between calculated and experimental patterns. On the other hand, the Rietveld refinement is an approximation for nanocapsular shapes and other known structures when the lattice

parameter c is the only parameter used to describe the unit cell.[46]

During the structural transformation, crystal changes can take place. For instance, ZrO_2 structures with tetragonal nature and partial stabilization were identified. Crystal changes can lead to formation of metallic clusters, promoting the redox properties.[47]

CuO species with crystallite sizes between 5–20 nm were also found. After sonication of Pd, the Pd−Cu structures presented cubic nature. The PCZT sample showed defined structure, at hkl (001) and hkl (111) and crystallites sizes of 11 and 6.5 nm. Only one peak at hkl (001) was detected for CZA, with crystallite size of 4.7 nm (Cu/ZrO_2-Al^{+3}). It is important to stress that the PCZA sample presented different structures, suggesting defects, such as Cu_3Pd clusters at $2\theta = 32°$, 35°, 51° and 54.0°; PdO_2 at $2\theta = 28.19°$; CuO at $2\theta = 24.53°$, 33.09°, 25.80° and Cu_2O cluster at 29.90°.[48] The in situ XDR results showed metallic particles at $2\theta = 40.02°$ and 47°, relative to Pd (111) and Pd (200) phases on the PCZA sample,[49] as shown in Figure 2. This suggests weak interactions of Pd with the ZrO_2
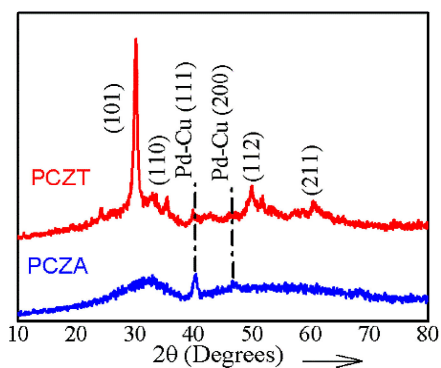

Figure 2. XDR Profiles of Pd−Cu reduced samples: PCZA and PCZT.

support and the existence of copper clusters, which facilitate the Pd reduction from cubic structure. Furthermore, the reduced PCZA sample contained more faceted palladium lattice (111) due to many levels of exposed Pd. This was attributed to the differences between the crystal size found for Pd (111) lattice. On the other hand, the PCZT sample displayed the Pd (111) phase, suggesting that the metallic Pd particles migrated to the surface during the reduction process. It seems that the metallic Pd particles were formed during the calcination step for the Pd−Cu catalyst.

Thermal Stability and Reducibility of Pd−Cu Catalysts

Figure 3 (b) shows the TPR profiles of Pd−Cu catalysts and Pd-free Cu/ZrO_2 modified catalysts. Figure 3 (a) shows the TGA and DTA results of the samples containing copper supported on CZA ($Cu/ZrO2-Al^{+3}$) and CZT ($Cu/ZrO2-Ti^{+4}$). The sol-gel materials showed weight loss of water and hydroxyl groups, which can be attributed to the alkoxide anions released from the sol-gel precursors. The weight loss varied between 20 and 40%,

with endothermic peaks at 72°C and 90°C caused by hydroxylation and dehydration. [50] Significant differences could be detected between these two samples.

The CZT (Cu/ZrO_2-Ti^{+4}) sample showed two endothermic peaks at 430 and 640°C, which can be assigned to structural modification and complete collapsed structure,[51] respectively. On the other hand, the CZA (Cu/ZrO_2-Al^{+3}) sample evidenced two endothermic peaks at 191.2 and 342°C, which can be assigned to structural changes, probably due to the incorporation of copper inside the ZrO_2 modified structure.[52] These effects can eventually affect the metallic reduction. Four peaks could be observed, suggesting the occurrence of different structures, which can be related to the presence of different kinds of copper species, like Cu^{+2} in solid solution at 323 and 314°C, bulk CuO at 381°C and highly dispersed nano-CuO at 175°C.[39,53,54] The TPR profiles suggest that the Pd−Cu cubic structure promotes the reduction of palladium at low temperatures. The PCZA samples showed Pd reduction at room temperature and at 246 °C, attributed to isolated Pd on ZrO_2 support.[55] On the other hand, the PCZT sample showed reduction from room temperature until 246°C, suggesting stronger metal-support interactions and the reduction of copper species at lower temperature.[56]
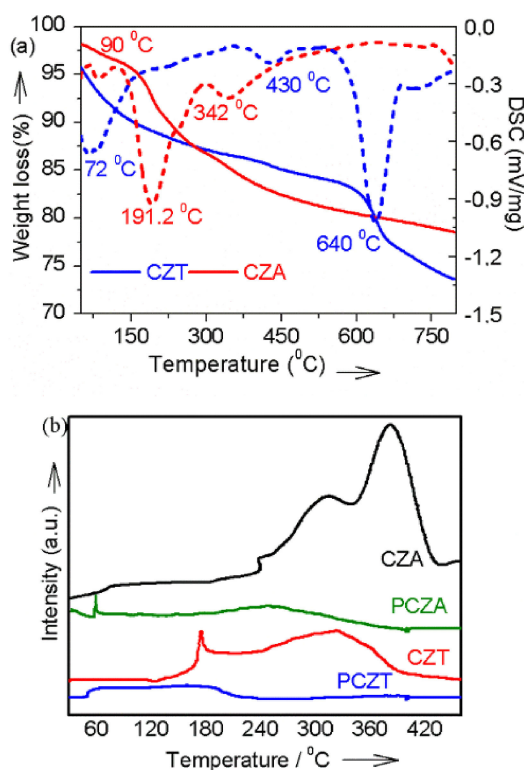

Figure 3. (a). TGA-DTA analyses of the CZA (Cu/ZrO_2-Al^{+3}) and CZT (Cu/ZrO_2-Ti^{+4}) monometallic copper catalysts (b). TPR profiles of Cu and Pd−Cu catalysts.

Scanning Electron Microscopy (SEM) and Transmission Electron Microscopy (TEM)

Images of the Pd–Cu supported on ZA and ZT (PCZA and PCZT) samples are shown in Figure 4 and indicate ordered materials with nano-spheroidal morphology.
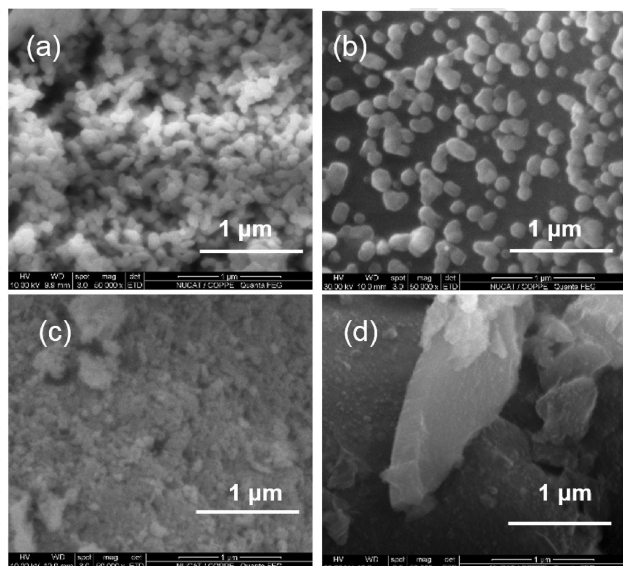

Figure 4. Scanning electronic microcopy of the Pd–Cu/ catalysts: (a) CZT, (b) PCZT, (c) CZA, (d) PCZA.

This morphology is probably due to the implosion of bubbles during the sonochemical process.[19] The promoted Ti^{2+} catalyst showed a more ordered structure than the promoted Al^{3+} version of the PCZA sample, which presented agglomerated particles. In fact, when palladium is incorporated, the catalyst structure undergoes changes that affect the catalyst morphology. Figure 5a,c) shows the TEM images of PCZA and PCZT samples, whereas Figure 5(b,d) shows the size distributions of the Pd–Cu particles.

TEM analyses revealed that the PCZA sample showed particles of similar sizes and shapes and are well distributed over the ZA support. The mean particle sizes are predominantly 42 nm. The particle size distribution varied between 30 and 45 nm. On the other hand, the PCZT sample showed non-homogeneous particle sizes and distributions, varying between 20 and 60 nm. Three distinct regions with different particle size distributions could be observed. Small particles are of the order of 5 to 20 nm and are observed in the first region, while larger particles varied between 50 and 80 nm in the third region. The second region showed two predominant mean particle sizes of the order of 30 and 42 nm, respectively. Figure 6 shows the high-resolution images (HRTEM) of metallic particles of the PCZT sample, with the corresponding Fast Fourier Transform (FFT) results, which correspond to the reciprocal space of the cubic crystallographic structure of the Cu–Pd solid solution.

Different crystal orientations can be observed. Figure 6 (b) shows the (001) face, while Figure 6 (d) shows the (111) face.
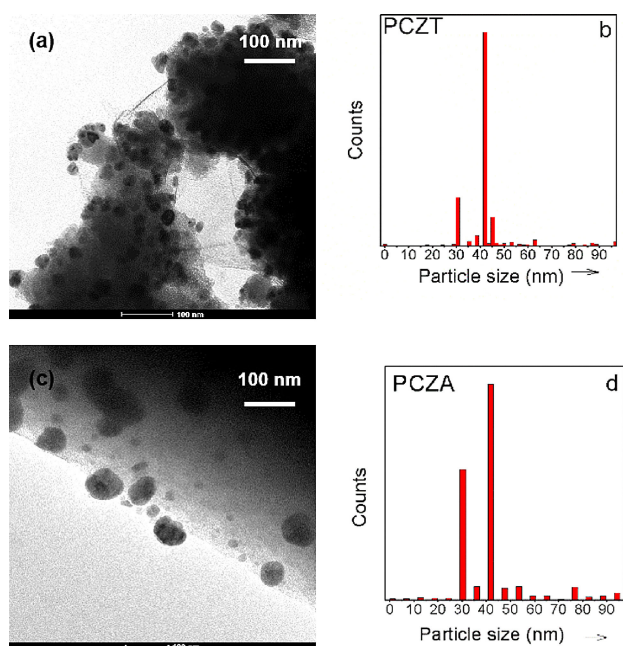

Figure 5. TEM Bright Field image (a) PCZA (c) PCZT and size distribution of samples PCZA (b) and PCZT (d).
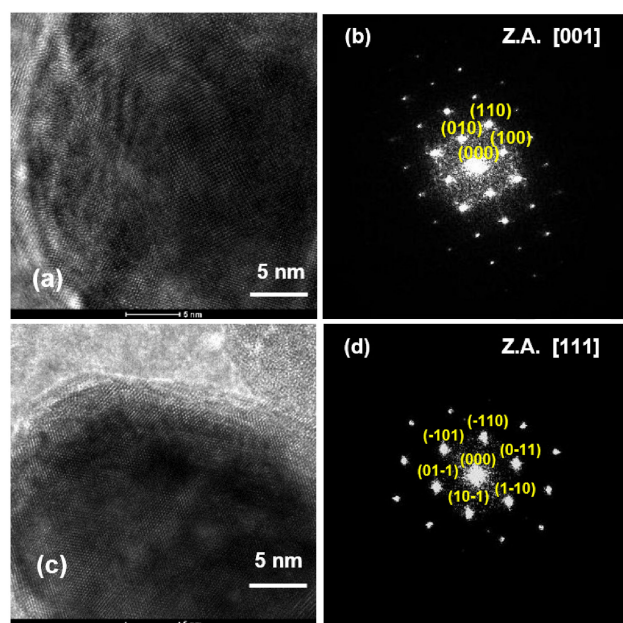

Figure 6. (a) HREM particle Pd/Cu (001) image of PCZT (b) FFT of particle Pd/Cu (001) PCZT (c) HREM particle Pd/Cu (111) image of PCZT (d) FFT of particle p2 Pd/Cu (111) PCZT.

The metallic particles of the PCZT catalyst are usually mono crystallites. Figure 6 shows the high-resolution images (HRTEM) of the metallic particles of the PCZA catalyst and Figure 7 shows the EDS spectra of the samples. The PCZA catalyst are more faceted, as shown in Figure 7 (b).

The EDS spectra for PCZT and PCZA samples displayed in Figure 6(b,d) and Figure 7b, respectively, are shown in Figure 8, and suggest the co-existence of particles with different Cu/Pd
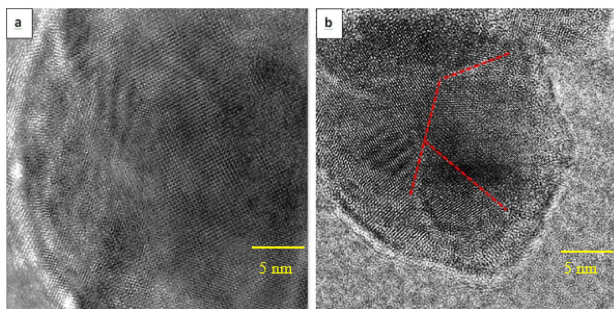
Figure 7. (a) Cu–Pd particle in PCZT (b) Cu–Pd particle in PCZA.

atomic ratios. Spectra (a) and (b) in Figure 8 show, respectively, Pd and Cu species, suggesting Cu_2Pd, Cu_3Pd and CuPd compounds, confirming the XRD results and in accordance with the literature.[33,35] Spectrum (c) indicates preferentially Pd particles.
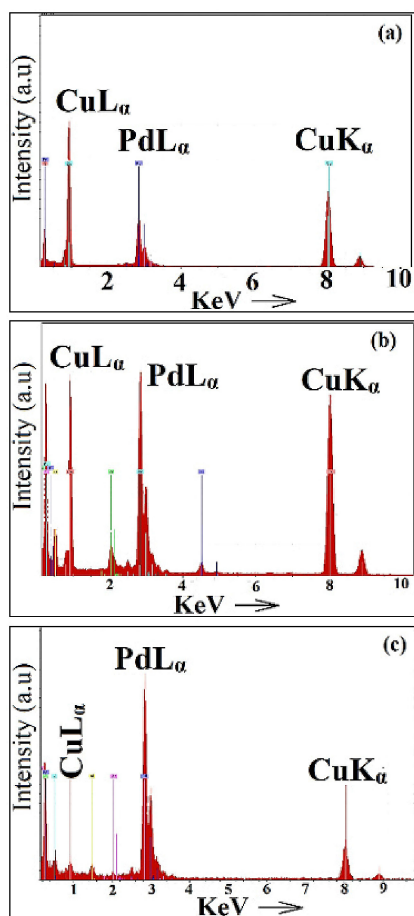

Figure 8. EDS spectra of catalysts (a) from Figure 6b, (b) from Figure 6. Adsorption-desorption isotherms of Pd–Cu catalysts and pore size distribution (b): PCZT (blue line), PCZA (red line).

Textural Analysis, Composition and Crystal Size

PdCu catalysts exhibited isothermals of type IV (Figure 9). Interestingly, the presence of Al^{+3} and Ti^{+4} ions promoted the
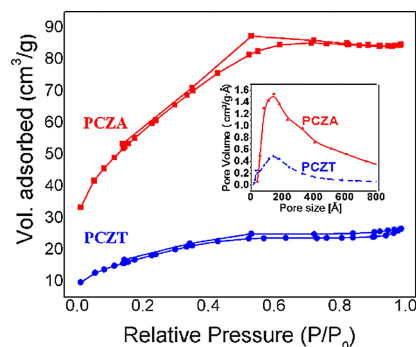

Figure 9. Adsorption-desorption isotherms of Pd-Cu catalysts and pore size distribution (b): PCZT (blue line), PCZA (red line).

structure by increasing surface areas, when compared to pure ZrO_2. All samples exhibited hysteresis; however, the ZrO_2 promoted with Ti^{+4} showed ordered mesoporous. The mean sizes of the pores of both samples were around 200 Å, as shown in Figure 9.

Table 2 presents the textural properties of ZrO_2-based catalysts, also presenting Pd and Cu crystallite structures and x-ray fluorescence results (XRF)

TEM analyses showed particle sizes of 5 nm, in agreement with the in situ XRD data, between 5.6 to 10 nm. The Pd/Cu atomic ratio influenced the distribution of the active sites and the values were very similar. The difference between them can be explained by phase transformations suffered during soni-cation.[26] Indeed, the morphology of these materials can change quickly, affecting the final composition.[58]

Temperature-Programmed Surface Reaction (TPSR)

Figure 10 displays the TPSR profiles of the PCZA and PCZT catalysts after reduction at 258 °C, respectively.

Both catalysts PCZT and PCZA reduced at 258 °C displayed significant differences, as shown in Figure 10. PCZT catalyst (Figure 10a) shows that the reaction started at 250 °C, with the consumption of O_2, AcOH and C_2H_4, prevailing the formation of CO_2 and H_2O. One must notice that the prevailing formation of CO_2 and H_2O indicates the partial combustion of acetic acid or ethylene, as shown in Equations (1) and (2)

$$C_2H_4O_2 + 2O_2 \rightarrow 2H_2O + 2CO_2 \tag{1}$$

$$C_2H_4 + 3O_2 \rightarrow 2H_2O + 2CO_2 \tag{2}$$

However, it is important to note the appearance of VAM, with maximum formation at 350 °C, followed by reduction of CO_2 and H_2O contents and formation of H_2. This suggests the

Table 2. Crystal structure, composition and textural properties for Pd–Cu catalysts[c].

	Size [nm]			A [m²/g]	V_P [cm³/g]	Pd [nm]	
Sample	d_{001}	d_{110}	d_{111}			Pd°$_{XRD}$[a]	Pd°$_{TPD}$[b]
PCZT	11	5	6.7	61.4	0.03	5.6	2.08
PCZA	4.7	–	–	201.5	0.13	10	2.27
Sample	Pd	Cu	Zr	O_2	Ti	Al	Pd/Cu
PCZT	1.27	2.73	42.89	31.07	23.04	0.00	0.44
PCZA	1.72	2.70	49.92	31.26	0.00	14.40	0.38

[a] Calculated after reduction with H_2; [b] Calculated from Equation (8) and (9). Pd$_{TEM}$ = 5 nm; [c] Empirical equation for samples: Pd$_{0.5}$CuO$_{10}$Zr$_{1.97}$Ti$_{2.2}$O$_8$ (PCZT) and Pd$_{0.5}$Cu$_{1.31}$O$_{15}$Zr$_4$Al$_{1.1}$O$_{1.1}$ (PCZA).

occurrence of partial oxidation and reverse shift reaction. [59] On the other hand, the PCZA catalyst under similar reduction condition (Figure 10(b)), showed high consumption of O_2 and consumption of AcOH at 200 °C, with simultaneous formation of CO_2 and H_2O. However, there is a continuous and significant formation of VAM, when compared to the PCZT catalyst, with maximum formation around at 330 °C and increasing formation of H_2O, CO_2 and H_2 up to 400 °C. This can be attributed to the reverse shift reaction. [60] The ethylene signal showed very low rates of consumption with the increasing temperature in the analyzed range (not shown).

TPD of CO

CO desorption results indicate the presence of surface Pd sites with increasing temperature, as shown in Figure 11. It is important to observe that the catalysts present different CO desorption profiles and formation of CO_2.

The CO desorption profiles present a maximum peak around 70 °C, which corresponds to the CO adsorbed and desorbed on metallic Pd°, in agreement with the literature.[59] The catalyst PCZA indicates a shoulder around 200 °C, attributed to desorption on Cu sites.[61] This shoulder was not observed on the PCZT catalyst, indicating no significant metallic copper at the surface. On the other hand, one can observe that the CO_2 profiles on both catalysts show different desorption peaks. The PCZT shows two peaks of desorption at 80 and 150 °C, while the PCZA presented only one pronounced peak at 180 °C. These results indicate the presence of secondary reactions, in particular the decomposition of CO on the PCZT and probably the water-gas shift reaction at higher temperatures, very significant on the PCZA catalyst. Thus [Eqs. (3)–(4)]:

$$2CO \rightarrow C + CO_2 \tag{3}$$

$$CO + H_2O \rightarrow CO_2 + H_2 \tag{4}$$
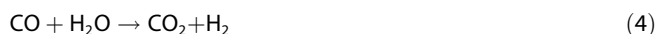
The presence of water can be observed in Figure 11 and can be assigned to the presence of hydroxyl groups of different nature at the surface. This fact justifies the decomposition of CO and occurrence of the shift reaction, with the formation of C at the surface and CO_2 and H_2 in the gas phase. Although the presence of water could be observed, it was not possible to detect H_2 during the TPD experiments due to the low intensity of the signal, when compared to CO, H_2O and CO_2 signals.
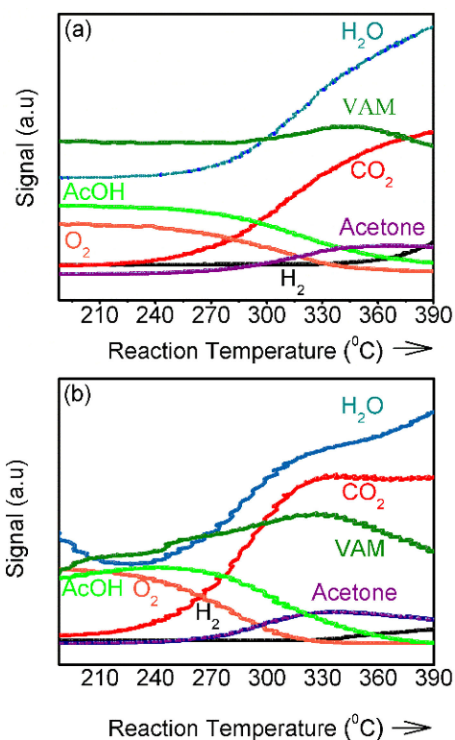

Figure 10. TPSR results at atmospheric pressure for PCZT(a) and PCZA (b) samples: (0.55 g/9.61 ml/min C_2H_4/1.25 9.61 ml/min O_2/ Ts = 24.5 °C (2 % AcOH).
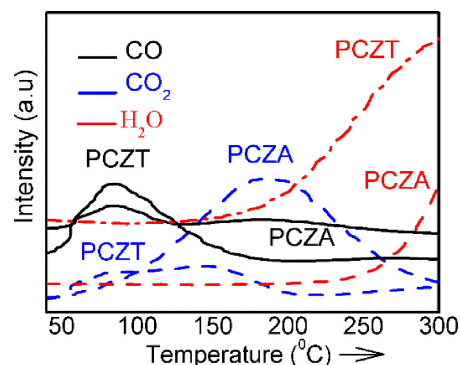

Figure 11. TPD of CO on Pd–Cu catalysts: CO_2 evolution (Blue lines), H_2O evolution (Gray lines). CO Desorption (Black lines).

The TPD results suggest that the acid AcOH dissociates to form CH_3^+ radicals and COOH fragments that may immediately be transformed into CO and hydroxyl groups or be oxidized with sub-surface oxygen[60] that can promote preferentially the formation of CO. In contrast, if the amount of sub-surface oxygen in the lattice is small, the methyl groups tend to form CO_2 [Eqs. (5)–(7)].[62] < ffr5

$$CH_3^+ + 2\left[O_s^{2-}\right] \rightarrow CO + 3OH^- \tag{6}$$

$$CH_3^+ + \left[O_s^{2-}\right] \rightarrow CO_2 + \frac{3}{2}H_2 \tag{7}$$

The PCZT catalysts exhibited one peak for Pd active sites, related to the lattice oxygen and hydroxyls groups at the surface, whereas PCZA catalyst showed low CO desorption attributed to low lattice oxygen, with simultaneous CO_2 formation. In fact, Cu presents different oxidation states (CuO, Cu_2O), interacting with the support, forming bimetallic species of $PdCu_x$ and thus copper clusters at the surface,[63] maintaining the sub-surface oxygen, which inhibits the PdC_x formation, facilitates the O adsorption and promotes H_2 spillover.[64] This is a remarkable characteristic of the PdCu alloy for acetoxidation, favoring the AcOH dissociation and the electron transfer from support to $PdCu_x$.[65] Moreover, the in situ XRD results revealed the presence of two Pd faces (111) and (200), as shown in Figure 2.

The metallic Pd promotes the C_2H_4 and AcOH coupling and minimal combustion. However, the presence of Cu^{+2} species, interacting with the support and Pd, promotes the formation of lattice oxygen that, with hydroxyl groups, favor the dehydrogenation of hydrogenated vinyl acetate.[66,67]

On the other hand, Cu^{+2} increases the probability of combustion of AcOH and C_2H_4, while the hydroxyl groups from support and $Cu+$ ions favor the formation of sub-products, like acetone, methane, and acetaldehyde at higher temperatures, reducing the selectivity towards VAM. In fact, the advantage of alloying with Cu is the electronic and ensemble effects for the production of VAM.

Catalytic Activity Tests

The catalytic tests were carried out for both catalysts and for different reaction conditions. Table 3 shows the AcOH and O_2 conversions for different gas hourly space velocity (G) (15.06, 15.92 and 22.86 $m^3/(h.kg_{cat})$) and temperatures of 150, 180 and 200 °C. The ethylene conversion did not suffer relevant changes, probably due to the low coverage of ethylene on Pd surfaces at atmospheric pressure, in accordance with Stacchiola et al.[68] Results show that the highest conversion was obtained at 200 °C for the PCZT catalyst, decreasing with increasing space velocity. It is important to observe that the PCZA sample exhibited the highest conversion for higher space velocity at 200 °C. The PCZT catalyst structure presents a cubic structure, which can influence the O_2 conversion and the diffusion into vacancies, transporting superficially the oxygen from the lattice

Table 3. AcOH and O_2 conversion as a function of GHSV over PCZT and PCZA catalysts at 150, 180 and 200 °C.

T(°C)	15.06[*] PCZT X_{AcOH}	X_{O2}	15.06[*] PCZA X_{AcOH}	X_{O2}	15.92 PCZT X_{AcOH}	X_{O2}	15.92 PCZA X_{AcOH}	X_{O2}	22,85 PCZT X_{AcOH}	X_{O2}	22,85 PCZA X_{AcOH}	X_{O2}
150	5.0	3.8	18.7	1.8	11.1	5,5	17.0	4.7	15.0	2.6	4.0	1.8
	5.0	3.5	18.4	1.8	11.0	5.8	16.8	4.3	15.2	2.1	3.8	1.6
	5.2	3.5	18.3	1.6	11.2	5.8	16.6	4.2	14.3	1.8	3.4	2.1
180	4.3	5.3	17.9	1.5	6.5	15.9	19.9	7.5	6.9	6.8	7.3	2.7
	4.5	5.3	17.3	1.5	6.3	15.5	20.1	7.5	6.5	6.1	8.0	2.7
	4.7	5.3	18.0	1.5	6.3	15.7	20.3	7.5	6.4	6.1	7.7	2.8
200	6.3	3.4	72.1	68.6	6.3	50.0	33.0	17.7	62.8	23.5	13.7	57.3
	6.1	3.9	72.2	68.4	6.6	50.2	32.6	17.7	62.3	22.6	14.2	58.1
	6.4	3.8	72.6	68.4	6.9	50.2	32.5	18.0	61.6	23.0	14.1	58.0

T(°C)	15.06[*] PCZT X_{ethy}	15.06[*] PCZA X_{ethy}	15.92 PCZT X_{ethy}	15.92 PCZA X_{ethy}	22.85 PCZT X_{ethy}	22.85 PCZA X_{ethy}
150	3.1	3.4	5.7	14.4	4.7	3.4
	3.6	3.3	5.5	14.5	4.8	3.7
	3.7	3.1	5.2	14.6	4.4	3.9
180	3.6	1.2	1.4	16.3	19.5	7.03
	3.9	1.7	1.5	16.2	18.6	6.98
	3.7	1.5	1.2	16.3	19.4	6.97
200	3.5	39.6	9.0	14.0	6.1	12.8
	3.7	39.6	8.5	13.8	6.6	12.8
	3.7	39.3	8.6	14.9	6.4	12.9

[*] The units for GHSW are given in $m^3/h*Kg_{Cat}$.

and therefore favoring the coupling with ethylene and AcOH intermediates. This is reinforced from the oxygen storage capacity measurements on PCZT and PCZA, respectively, 272 µmols O_2/g_{cat} and 155 µmols O_2/g_{cat}, indicating the presence of oxygen in the sub-surface lattice.[59] Catalytic results showed that at 200 °C and some specific conditions, the AcOH showed high conversion, due to AcOH combustion. For higher gas space velocity, the conversion increases for the PCZT samples Probably, acetic acid reacts with C_2H_4 and forms acetoxy species, which correspond to the cleavage of C—C and C—O bindings at the interface and the formation of intermediate species on Pd-Acetate,[69–70] The conversion of AcOH was higher for PCZA catalyst at 15.06 $m^3/h*Kg_{Cat}$. The loss of selectivity for PCZA samples is attributed to the formation of sub-products like CO and CO_2.

The catalyst PCZT presented better activity and selectivity than the PCZA catalyst, as shown in Figure 12. Han et al[59] showed that for temperatures up to 180 °C the combustion predominates; however, the AcOH concentration and space velocity GHSV may influence the products distribution simultaneously. Kuhn et al[69] showed that the selectivity to VAM is affected by the $O2$ conversion and particle size.[68,70]

It seems that the sub-surface oxygen atoms and hydroxyl groups promote the selectivity, which is consistent with the present results, suggesting that the PCZT catalyst promotes the formation of surface oxygenated species containing hydroxyl groups, increasing the VAM selectivity. Chen and Goodman claimed that the face (111) of palladium favors the activity when the palladium coverage of the nearest neighbors is maximized, meaning that nano-ordered materials could promote the concentration of surface active sites.[71]
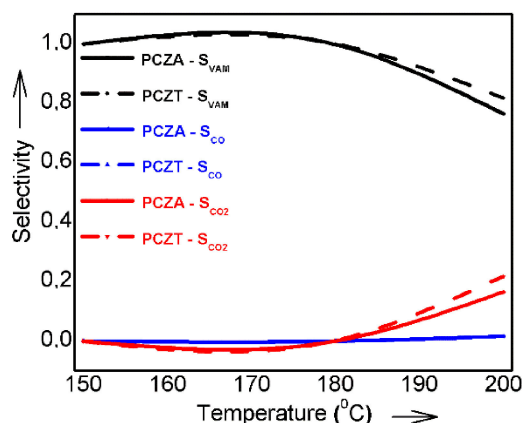
Figure 12. Selectivity at reaction conditions for GHSV = 15.92 m3/Kg*h for PCZT and PCZA catalysts.

X-Ray Photoelectron Spectroscopy (XPS)

These experiments were performed to examine the surface properties and the presence of metallic oxide phases of the different catalyst. The self-reorganization of Pd active sites depends on an electron donor from the support. Figure 13
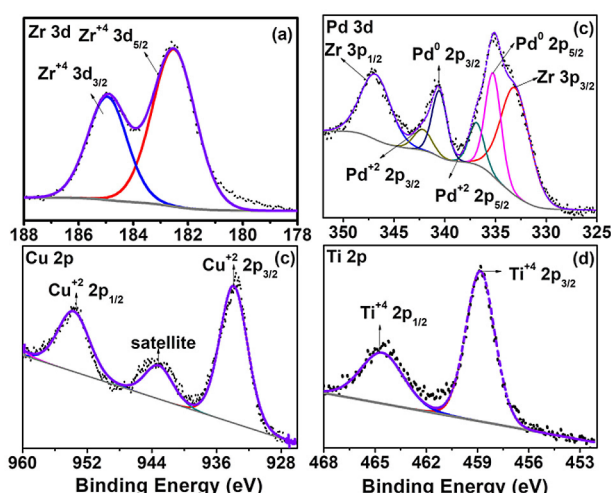

Figure 13. The X-ray photoelectron spectroscopy (XPS) patterns of: (a). Zr_3d signals (b), Pd_3d and Zr_3p (c), Cu_2p (d) Ti 2p.

exhibits the XPS spectra of the binding energies of Zr (a), Pd(b), Cu(c) and Ti(d) of the PCZT catalyst.

Figure 13a shows the oxidation states for Zr species on PCZT sample. The Zr^{+4} species are related to ZrO_2.[72–73] For the PCZT sample, the curve fitting results at 182.4 eV ($3d^{5/2}$) and 184.8 eV ($3d^{3/2}$) are related to the spin-orbit splitting of the Zr $3d$ band, relative to Zr^{+4}. The tail at the low energy side of the Zr 3d spectra can be either related to a minor contribution from reduced Zr species or changing in the coordination number of zirconium due to the interactions with the other elements. The binding energies of the different species at the surface are presented in Table 4.

Table 4. Binding Energy and chemical composition for PCZT sample.

Transition	BE [eV]	FWHM [eV]	[% Atomic]	Assignment
Zr 3d$_{5/2}$	182.3	1.86	48.9	Zr^{+4} in ZrO_2
Zr 3d$_{3/2}$	184.7	1.63	42.7	Zr^{+4} in ZrO_2
Ti 2p$_{3/2}$	458.83	2.00	49.7	Ti^{+4} from zrilankite (TiZr)Ox
Ti 2p$_{1/2}$	464.68	2.95	50.2	–
Cu 2p$_{3/2}$	933.87	3.97	40.8	Cu^{+2} from CuO
Cu 2p$_{1/2}$	953.67	4.51	39.7	–
Pd 3d$_{5/2}$	335.49	2.47	11.5	Pd° reduced from PdO
Pd 3d$_{3/2}$	340.84	1.99	10.0	–
Pd 3d$_{5/2}$	338.57	2.47	1.8	Pd^{+2} from PdO
Pd 3d$_{3/2}$	344.29	1.99	1.59	–
Zr 3p$_{3/2}$	333.19	3.87	37.9	Zr^{+4} from ZrO_2
Zr 3p$_{1/2}$	346.91	3.18	37.07	–
Pd/Cu ratio	1.98	–	–	–
Zr/Ti ratio	1.57	–	–	–
Elemental analysis [%]				
Pd 3d	Cu 2p	Ti 2p	Zr 3d	O 1 s
10.936	5.52	8.16	12.8	62.50

The difference between the bands at Pd 3d$_{3/2}$ and Pd 3d$_{5/2}$ (5.6 Ev) indicates the presence of metallic Pd^0 and Pd^{2+}, corresponding to the binding energies Pd^0 3d$_{5/2}$(335.2 eV, FWHM 1.84 eV); Pd^0 3d$_{3/2}$ (340.5 eV) Pd^{+2} 3d$_{5/2}$(336.86 eV, FWHM 1.74 eV); Pd^{+2} 3d$_{3/2}$ (342.16 eV) respectively,[72,73] probably due to the activation conditions at room temperature, favoring the formation of stable bimetallic structures. The binding energy and satellite peaks for Cu 2p$_{3/2}$, correspond to ions of the oxide, as shown in Figure 13c for the PCZT sample. The surface atomic ratio of Pd/Cu is 1.98, which means that Pd is almost the double of Cu. The surface Zr/Ti ratio is 1.6, indicating higher content of Zr at the surface. Finally, the metal loadings of Pd (1.49) and copper (3.04) at the surface are very close to the experimental values, which in fact shows the charge balance between the $ZrTiO_x$ support and the Pd metallic surface.

Apparently, a low fraction of the Zr species can be oxidized, moving from support to the surface, which can be easily oxidized, to compensate the loss of hydroxyls groups. The results showed that these structures would be useful for the acetoxidation reaction, mainly due to the presence of the superficial oxygen and $PdCu_x$ active sites, promoting vacancies in the sub-surface layers of modified ZrO_2, facilitating the hydrogen spillover in hydrogenation and dehydrogenation reactions.[74,75]

DRIFT Spectroscopy

The in situ IR analyses revealed the presence of surface intermediates related to ethylene coupled on Pd active sites, with symmetrical stretching (C—H). (C—CH$_3$) at 950, 2988, 1031 and 1047 cm^{-1}. These bands suggest the ethylene dehydrogenation step and AcOH coupling.[9,10,68] Moreover, the AcOH typically adsorbs at 1346 cm^{-1}, due to AcOH stretching (COO).

In addition, AcOH shows three types of stretching (C=O): monomeric $(Pd(OAc)_4)^{2-}$ at 1776 cm^{-1}, dimeric species[9,76] $(Pd_2(OAc)_6)^{2-}$ at 1732 cm^{-1} and trimeric species $(Pd_3(OAc)_6)$ at 1462 cm^{-1}, as shown in Figure 14.

ing.[78] The IR spectra for PCZA and PCZT catalysts after 1 h reaction were compared for three temperatures in the region of AcOH intermediates, for C—H and C—C stretching, appearing in Figure 15.
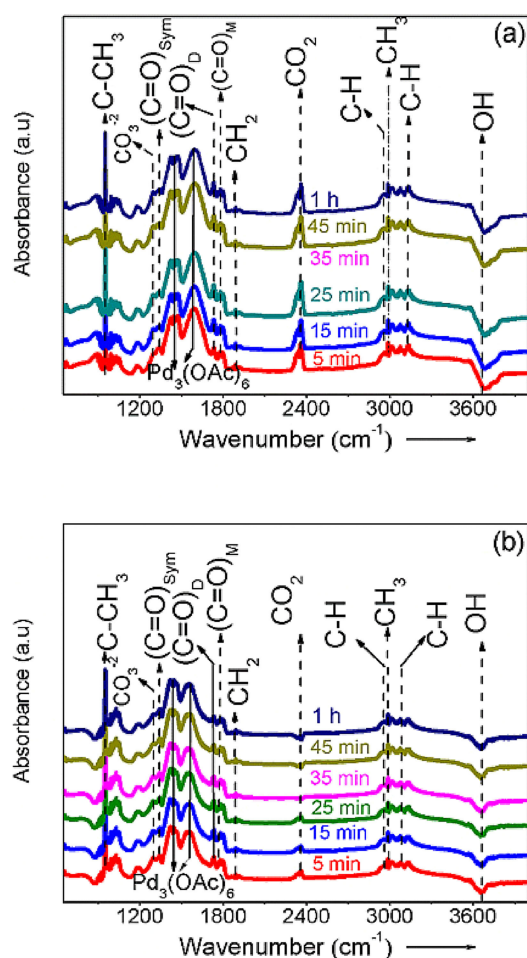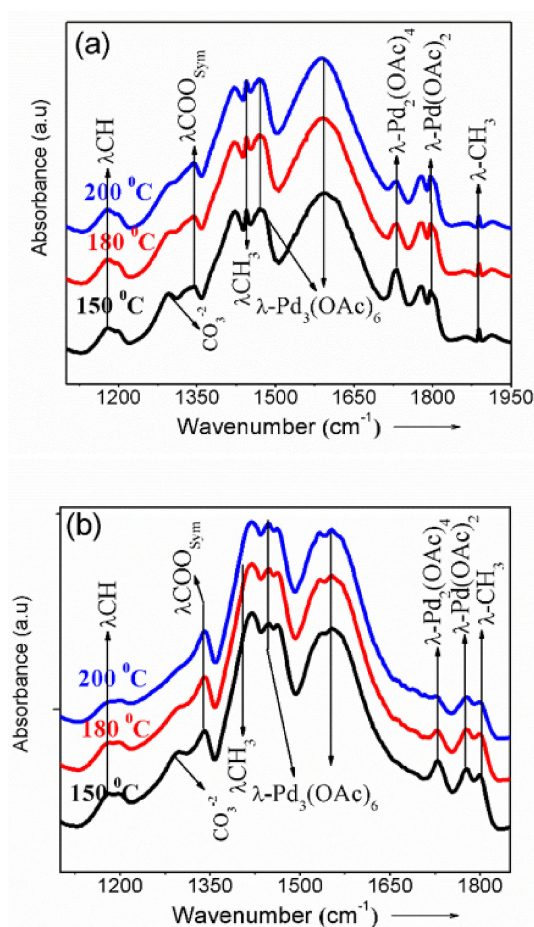

Figure 14. In situ IR spectra of PCZA (a) and PCZT (b) catalysts. Conditions: 2 % AcOH, 1 ml/min O_2/10 ml, C_2H_4/Balance with He 70 ml/min, P = 1 Bar at 150 °C.

Figure 15. IR spectra of surface intermediates for AcOH and C_2H_4: 1 h reaction test. Conditions: 2 % AcOH, 1 ml/min O_2/10 ml C_2H_4/Balance He 70 ml/min. P = 1 Bar, T = 150, 180, 200 °C. (a) PCZA sample, (b) PCZT sample.

The C—C stretching band at 1191 cm^{-1} was assigned to C_2H_4 deformation that precedes the bands at 950 and 1031 cm^{-1}. The CO_2 stretching appears at 2340 cm^{-1}, showing higher formation on the PCZA catalyst (see Figure 14(a)). On the other hand, for the PCZT catalyst (see Figure 14(b)), CO_2 stretching adsorption bands were found in the first 15 minutes. Later, the peak decreased in the same region, indicating the CO_2 formation. The symmetric bands assigned at 1303 cm^{-1} correspond to ionic carbonate bands,[77] due to the CO adsorption. For the PCZA catalyst, this stretching was more pronounced, affecting AcOH adsorption on the active site. Thus, for PCZT catalyst this stretching disappeared after 1 h reaction. In agreement with the CO —TPD (Figure 11), this confirms that the Pd sites of the PCZT sample present higher CO desorption, without prejudice of the AcOH coupling. At last, the terminal hydroxyls were detected at 3675 cm^{-1}, assigned to the Zr-OH stretch-

Figure 15 shows that the stretching bands for Pd(AcOH) intermediates $(v\text{-}(Pd_3OAc)_6)$, $v\text{-}(Pd(Oac)_4)^{2-}$, $v\text{-}(Pd_2(Oac)_6)^{2-})$ are more pronounced for the PCZA (Figure 15a) catalysts. However, the symmetrical stretch band (COO) is more pronounced for the PCZT catalysts (Figure 15b). Lercher et al[9] claimed that there is a competitive mechanism between O_2 adsorption and PdAcOH intermediate formation, which occurs when the C=O stretching decreases. $(Pd_3Oac)_6$ tends to form dimers and monomers of Pd, which favor the AcOH combustion on the actives sites. For PCZT and PCZA catalysts, a slight decrease of this stretching was observed at temperatures up to 150 °C, followed by the CO_2 formation. Apparently, the PCZA active sites enable the stability of Pd intermediates. However, the produced CO_2 was adsorbed over the catalysts whereas the PCZT catalyst showed a decreasing peak for CO_2 intermediate, which suggests that carbon consumption from C—C cleavage, attributed to surface oxygenation.

There is a competitive mechanism between the adsorption of oxygen and $Pd_3(OAC)_3$ formation (1424 cm^{-1}). which maintains the reaction dynamics between asymmetric and symmetric COO stretching (1586 cm^{-1}). The formation of intermediates in these nanostructures follows a reaction path that can be explained by the electron transfer between PdCu species with ZrO_2 modified and CuO ligand effects.[79] The detection of acetoxyethyl intermediate related to VAM hydrogenated at 1718 cm^{-1} was more significant for the PCZT sample (Figure 16
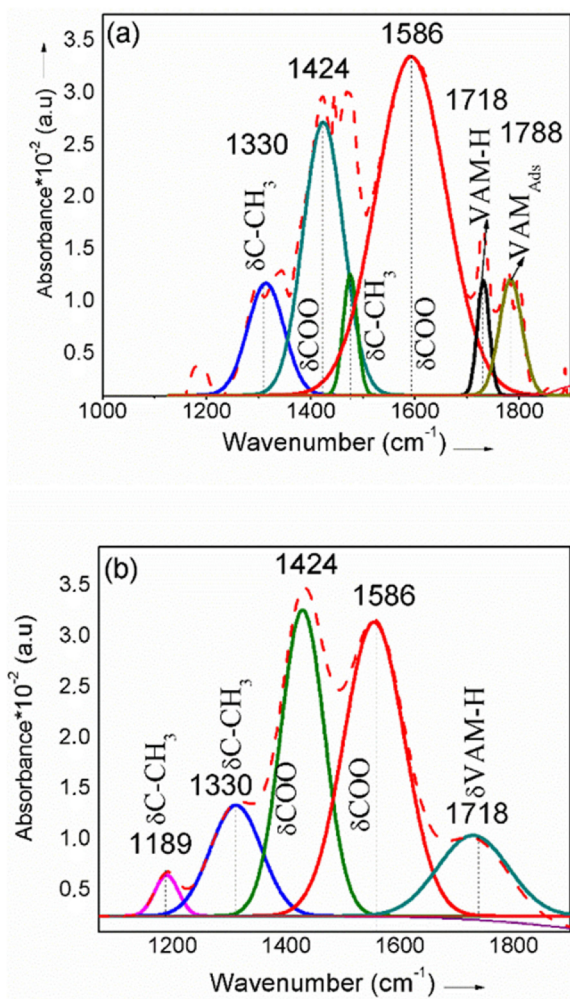

Figure 16. IR spectra collected during in situ reaction for VAM synthesis. Conditions: 2% AcOH, 1 ml / min O_2 / 10 mL C_2H_4 / Balance He 70 mL/min. P = 1 Bar, T = 150 °C. (a). PCZA sample (b). PCZT sample.

(b)). On the other hand, the additional peak for the PCZA sample that appeared at 1788 cm^{-1} (Figure 16(a)) is assigned to adsorbed VAM,[76] which means that β-H elimination step was not efficient and the VAM will be suffer derivatization. The presence of ethylene intermediates suggests the initial coupling of C_2H_4, O_2 and AcOH, over the active site, which characterizes the Samanos mechanism.[70] The coupling steps usually are faster than β-H elimination; however, for high values of the ethylene conversion the VAM selectivity is reduced due to the ethylene combustion. Therefore, when ethylene begins to

dehydrogenate on Pd active sites, it becomes active and, thus available for formation of surface intermediates, leading to VAM formation at 150 °C.

These results follow the reaction mechanism proposed by Stacchiola et al,[68] with ethylene and AcOH coupling steps favored by surface oxygenated groups and terminal hydroxyls groups. In agreement with Augustine et al[76] it suggests that the vinyl acetate-hydrated intermediates appears in the same region of Pd(AcOH) surface intermediates.

The nature of PdCu$_x$ active sites, the oxygen storage capacity (OSC) and the hydroxyl species presented on catalysts surface suggest the β-elimination of vinyl acetate from the surface, as proposed for the reaction steps in Scheme 1.[68,70] It
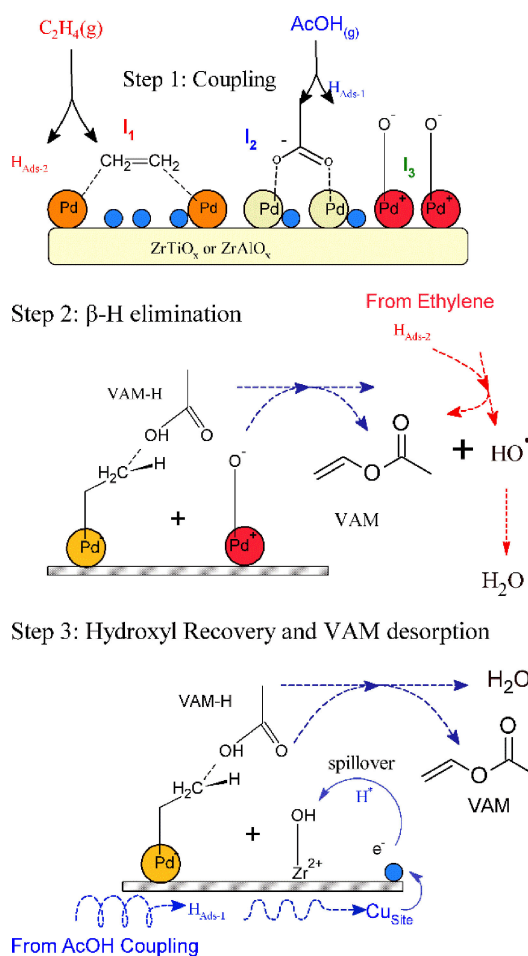
Scheme 1. Reaction pathway of ethylene acetoxidation over Pd–Cu/ZrO_2 based catalysis.

shows the surface hydroxyl groups, which allows the VAM desorption and H_2O formation. Indeed, the hydroxyl and oxygen coverage depend on the synergy between Cu/ZrO_2 species,[80,81] indicating that the hydroxyl species are regenerated. Furthermore, the Zr from support will be oxidized to hydroxyl surface groups. In agreement with the XPS results (Figure 13(a)) this lead to maintain the balance between hydroxyl groups involved in the reaction mechanism and the Zr

hydrated from desorbed water from VAM synthesis. In scheme 1, we propose the possible reaction path for VAM over PdCu catalysis.

Table 5. Intermediates and main species detected by DRIFT spectroscopy.

Species	Reaction step	Wavelength [cm^{-1}]
C—CH$_3$	C$_2$H$_4$ Dehydrogenation	950
C—H		2953
CH$_2$		1888
(C=O)$_{As}$	AcOH Coupling	1424
(C=O)$_{Sy}$		1586
(C=O)$_{Dimer}$		1732
(C=O)$_{Monomer}$		1776
(C=O)$_{Trimer}$		1462
CO$_3^{-2}$	CO$_2$ coupling	2340
Zr—OH	hydroxyl groups	3675
VAM	VAM and VAM Hydrogenated	1788
VAM-H		1718

In Table 5, are the main intermediates that were detected in DRIFT spectroscopy and represent as well, the reaction path of the Scheme 1 as Follow:

The IR spectra of Figure 16a showed that the limiting step of the reaction over the PdCu system was the desorption of VAM, as observed by the presence of VAM—H fragment that represent the dehydrogenation step without VAM desorption. The VAM—H band, related to VAM hydrogenated was not detected for the PCZT catalyst (Figure 16b). On the other hand, for the PCZA catalyst the VAM—H step occurred with posterior VAM desorption, being represented by the VAM adsorbed band, this explain the fact that over temperatures reaction up to 200 °C, will promote loss of selectivity and will exhibit higher conversions of AcOH for low O$_2$ conversion by the accelerated decomposition of the AcOH on the active sites at 15.92 m^3/h*Kg$_{Cat}$. In this case, a new reaction path will be achieved, without a dehydrogenation step, instead of H$_2$ spillover, which is responsible for promoting the ethylene acetoxidation. Pd—Cu complexes were used for VAM synthesis in homogeneous phase. As far as we know, there are not studies about the effects of metal-support interaction influencing the reaction, even for the PdAu catalyst. PdCu species over modified ZrO$_2$ support showed this synergy for the VAM synthesis. Copper clusters and isolated ions provided alloys with Pd, exhibiting unique properties, facilitating the reaction steps, due to the presence of oxygen vacancies in sub-surface clusters and OH at its interfaces, which are affected by the nature of support.

Conclusions

We investigated the catalytic synthesis of vinyl acetate from ethylene, acetic acid and oxygen on Pd—Cu catalysts supported on modified ZrO$_2$, using a sol-gel and sonochemical method. The Pd—Cu system showed different structures on modified ZrO$_2$ supports, like (Pd$_{0.5}$Cu$_{1.31}$O15Zr$_4$Al$_{1.1}$O$_{1.1}$) and (Pd$_{0.5}$

CuO10Zr$_{1.97}$Ti$_{2.2}$O$_8$), exhibiting monoclinic and tetragonal/ortho-rhombic structures.

Results also showed that copper species promoted the Pd reduction, influencing the electronic structure and vacancies at the interface of PdCu$_x$ with the modified ZrO$_2$ support. TPR results showed that copper species promoted the Pd reduction, and all these factors influenced the β-H elimination step

Structural characterization showed that Pd—Cu (111) and Pd—Cu (001) faces are better distributed on the PCZT than on PCZA catalyst. HRTEM results confirm these results. XPS results showed that the Pd—Cu(111) faces at the surface are predominant on the ZrO$_2$ modified with titanium. These structures favor the acetoxidation reaction, due to the presence of the superficial oxygen and the Pd and Cu active sites at the surface. Copper promoted the vacancy in the sub-surface layers, which facilitated the hydrogen spillover for the hydrogenation step. The PCZT catalyst presented higher VAM selectivity at 150 °C when compared to the PCZA catalyst under similar conditions. The PdCu faces exposed in PCZT samples minimize sub products formation and facilitate the O$_2$ mobility in Pd—Cu crystal structure.

DRIFTS results showed the presence of different intermediates, which suggest the presence of palladium acetate species, dehydrogenated ethylene species, terminal hydroxyls from ZrO$_2$ but not adsorbed AcOH and C$_2$H$_4$ species. Results identified palladium acetate species, ethylidyne and vinyl acetate species.

Experimental Section

Catalyst Preparation

ZrO$_2$-based catalysts were prepared via sol-gel method.[38,39] Ethanol (Aldrich, 99%) was initially refluxed for 15 min. Then, aluminum tri-sec-butoxide (Aldrich, 97%) was added and kept under mild stirring for 1 h. Afterwards, HNO$_3$ (Baker, 70%) was added dropwise under continuous stirring, producing a colorless solution. The solution was cooled to room temperature and acetic acid (Aldrich, 99.7%) was added. The entire solution was then cooled to 0 °C. In the following step, ZrO$_2$ n-propoxide (Aldrich, 70%) was added to the reacting system and kept under continuous stirring until room temperature for 24 h. Finally, deionized water was slowly added. The molar ratios of reactants were equal to: H$_2$O/(Zr + Al) = 2, HNO$_3$/ (Zr + Al) = 0.05, EtOH/ (Zr + Al) = 32.5, and Zr/Al = 1. Titanium n-propoxide (Aldrich, 99%) was refluxed with Ethanol (Aldrich, 99%) under constant magnetic stirring for 2 h. Then, the ZrO$_2$ n-propoxide (Aldrich, 70%) was added dropwise with HNO$_3$ (Baker, 70%) for 15 minutes, to keep the pH equal to 3. The solution was kept under constant stirring for 48 h. Finally, a solution of ethanol/water (83% EtOH v/v) was added for 1 h and dried for 24 h at 100 °C. The powders were transferred to a quartz reactor and calcined with pure air (150 cm^3/min) at 400 °C for 5 h. The molar ratios of reactants were equal to: H$_2$O/ (Zr + Ti) = 2, HNO$_3$/(Zr + Ti) = 0.21, EtOH/(Zr + Ti) = 32.5, and Zr/Ti = 1.

The obtained products were dried for 24 h at 100 °C and calcined in air at 400 °C for 5 h. Metals were impregnated by sonication, using a sonicator AUTOTONE SERIES (90 W) and irradiation time of 60 minutes for copper and 90 minutes for Pd.[40] Copper (II) acetylacetonate (97%, Aldrich) was dissolved in Ethanol (Aldrich 99%) and Palladium (II) acetylacetonate (99%, Aldrich) in chloroform (Aldrich, 99%). 100 mL of ethanol (Aldrich, 99%) was added

for dispersion of 3 g of the support during 1 h at room temperature. The copper solution was added dropwise. Wave pulses were used to avoid overheating and development of hot spots in the liquid.[19] The solids were dried at 100 °C for 24 h and calcined at 400 °C during 6 h, using air. After copper incorporation, the material was sonicated again with a solution containing the palladium precursor and the metal was incorporated using the same procedure. Finally, the solid powder was dried and calcined with He at 100 mL/min[41] for 6 h. The nominal composition was of 3% of Copper and 1.5% of Pd. Samples were labeled according to the support and metal used in each particular preparation as: (i) ZrO_2-Al^{+3} (ZA); (ii) ZrO_2-Ti^{+4} (ZT); (iii) Cu/ZrO_2-Al^{+3} (CZA); (iv) Cu/ZrO_2-Ti^{+4} (CZT); (v) Pd—Cu/ZrO_2-Al^{+3} (PCZA); and (vi) Pd—Cu/ZrO_2-Ti^{+4} (PCZT).

Catalyst Characterization

X-ray diffraction analyses were performed on a Rigaku Miniflex II analyzer (Delaware, USA), using copper radiation (CuKα $\lambda =$ 1.5418 Å) and scan parameters of $2° < 2\Theta < 80°$, 2°/min and 0.05°/step. The Rietveld refinement was performed, assuming that part of Al and Ti atoms occupy Zr sites in the tetragonal/cubic or monoclinic zirconia lattice,[42,43] besides the separate alumina (γ-Al_2O_3) and titanium phases (anatase, rutile). To investigate the crystalline structure of metallic Pd sites, the in situ X-ray diffraction measurements were performed at room temperature, under reducing environment at 300 °C, with a mixture of 10/90 v/v% H_2/He at 50 mL/min. The diffractograms of the reduced samples were obtained in a Rigaku, DMAX 2500 model diffractometer (USA), using copper radiation (CuKα $\lambda =$ 1.5418 Å) and scan parameters of $2° < 2\Theta < 80°$, 2°/min and 0.05°/step.

Temperature programmed reduction (TPR-H_2) measurements were performed in an Pilot Unit containing a thermal conductivity detector. PCZA and PCZT samples were pretreated in He (30 mL/min, at 150 °C for 1 h) and then switched to a 1.8/98.2 v/v% H_2/He at 30 mL/min flow, in the temperature range from 25 to 400 °C and heating rate of 10 °C/min.

Oxygen storage capacity measurements were performed in a microreactor coupled to a Quadrupole mass spectrometer Model Balzers-Pfeiffer QMS 200 (Asslar-Germany). Samples were reduced with H_2 at 400 °C for 1 h. Then, a 5/95 v/v% O_2/He mixture flowed through the catalyst bed until finishing the oxygen uptake. The reactor was purged with He and the dead volume was obtained by switching the gas to the 5/95 v/v% O_2/He mixture.

Temperature programmed desorption of CO was performed for determination of the surface sites. Samples were dried under He flow (50 mL/min) up to 200 °C, at a heating rate of 10 °C/min and then cooled to room temperature. First, the sample was reduced with 10/90 v/v% H_2/He (50 mL/min) up to 300 °C, at a heating rate of 10 °C/min and kept for 1 h at 300 °C, followed by cooling to room temperature with He flow. After reduction, the catalyst was exposed to a mixture of 5/95 v/v% CO/He flow (at 30 mL/min) for 1 h, at room temperature. Then, the non-adsorbed CO was removed with He flow. Desorption was carried out under He flow (50 mL/min) at 10 °C/min, from room temperature up to 300 °C. The CO, CO_2 and H_2O were analyzed with help of mass spectra signals Model Balzers-Pfeiffer QMS 200 (Asslar-Germany). The dispersion and particle sizes were determined using the following Equations (8) and (9):[44]

$$D_{ME} = \frac{20000 V_{CO} W_{ME}}{C_{ME}} \qquad (8)$$

$$d_{ME}(nm) = \frac{n}{D(\%)} * 100 \qquad (9)$$

where V_{co} is the CO uptake (mol/g_{cat}, C_{Me} represents the metal cross section (15 $Å^2$/at, for Pd), W_{Me} is the atomic weight of palladium (106.24 g/mol), "C_{Me}" is the metal loading (wt%), while n is 0.9 for Pd (nm).[44]

The chemical composition of the catalysts was evaluated by X-ray fluorescence, using a Rigaku Rix 3100 spectrometer (Texas, USA) and a rhodium tube as the X-ray source. The textural properties were obtained by N_2 physisorption in an ASAP 2020 (Micromeritics, Norcross USA) equipment. Samples were degassed at 300 °C for 24 h under vacuum before measurement.

Scanning Electron Microscopy (SEM) analyses were obtained by Field Emission on a Quanta 400 model (ThermoFisher, USA), operating between 10–20 KV and equipped with a Microanalysis EDS system. Samples were prepared by dispersion on a conductive film, adhered to the grid.

Transmission electronic microscopy (TEM) analyses were performed using a ChemiSTEM FEI Titan 80–200 field emission gun scanning transmission electron microscope (Oregon, USA) operating at 300 Kv accelerating voltage. The TEM samples were prepared by dilution of the solid in isopropanol and dropped on carbon coated copper grids at standard conditions for temperature and pressure. The high resolution TEM (HRTEM) mode was used to identify the crystal structures of the nanostructures. The elemental composition was determined by Energy dispersive x-ray spectroscopy (EDS) with an EDAX spectrometer in STEM mode.

XPS analyses were performed on a SPECH Equipment PHOIBOS 100/150 (SPECS Surface Nano Analysis GmbH, Berlin, Germany) with AlKa radiation (E = 1486.6 eV). Samples were distributed on a stainless-steel sample holder and fixed with a double adhesive carbon tape. The analyses were performed under vacuum (10^{-7} mbar). The electron binding energies were referenced and calculated for Ti_{2p}, Zr_{3d}, Al_{2p}, Cu_{2p} and Pd_{3d} bands, and fitted by Gaussian–Lorentzian curves after Shirley background subtraction.[45]

Temperature-programmed surface reaction (TPSR) were performed using samples of 500 mg of catalyst in a quartz reactor, dried under He flow at 50 mL/min and heated at 5 °C /min up to 200 °C, kept for 1 h and then cooled to room temperature. The catalysts were pre-reduced with 10/90 v/v% H_2/He at 50 mL/min, from room temperature up to 258 °C and subsequently at 400 °C, for reduction of Pd and Pd—Cu oxides, respectively. After reduction, the catalysts were cooled down to 150 °C in He atmosphere at 50 mL/min. The AcOH concentration was firstly adjusted with He flow at 132 mL/min through the saturator, maintained at 30 °C (2.83 kPa), bypassing the reactor during 1 h. Then, the gas mixture containing ethylene (9.61 mL/min) and 5/95 v/v% H_2/He flow (25 mL/min) was adjusted previously on the flow controller; the saturator was switched from the bypass to the reactor, at 266.6 mL/min. The reaction was performed by increasing temperature from 150 °C to 400 °C, at a heating rate of 5 °C/min. Reaction products were analyzed in the mass spectrometer (Model Balzers-Pfeiffer QMS 200, Aßlar, Germany). The following mass fragments were analyzed: C_2H_4 (m/z = 26.27), AcOH ((m/z = 45.60), O_2 (m/z = 16, 32), vinyl acetate (m/z = 15,43,86), water (m/z = 17,18), CO (m/z = 28), CO_2 (m/z = 44), H_2 (m/z = 2), methanol (m/z = 31), ethane (m/z = 30), ethyl acetate (m/z = 61,70,88), ethanol: (m/z = 29.46) and methyl acetate (m/z = 59.74).

Catalytic Tests

Ethylene acetoxidation reactions were performed in a quartz reactor under atmospheric conditions, varying the feed inlet for the bimetallic catalysts Pd—Cu catalysts on both supports ZA and ZT (PCZA, PCZT). Reactions were carried out with feed inlet mixture in

the ranges of AcOH (1.59–8.26 mol%), O_2 (2.8–8.8 mol%), C_2H_4 (7.8–37.6 mol%) and argon. The gas space hourly velocities (GSHV) were equal to 15.06, 15.92 and 22.80 $Nm^3/(h.kg_{cat})$. Initially, 500 mg of catalysts were reduced with pure H_2, from room temperature up to 300°C, at heating rate of 5°C/min. Afterwards, the samples were cooled with He to 150°C. The outlet gas stream was monitored by gas chromatography (CP-3110 Varian, Santa Clara, USA) equipped with two separation columns (Poraplot U, Carboxen 1006 plot) and two detectors (FID, TCD) for three temperatures (150, 180, 200°C). The individual conversions of the reactants (C_2H_4, O_2 and AcOH) and the selectivities in dry basis were calculated in accordance with Equations (10) and (11), respectively.

$$X_j = \frac{F_{j_0} - F_j}{F_{j_0}} * 100 \qquad (10)$$

$$S_j = \frac{F_J}{F_T} * 100 \qquad (11)$$

where F_j is the outlet molar flow of reactant j (C_2H_4, O_2 and AcOH); F_{j_0} is the inlet molar flow of reactant j (C_2H_4, O_2 and AcOH); F_T is the total flow and S_j is the selectivity for product

In situ DRIFT Spectroscopy

The in situ DRIFTS-MS analyses were performed on a Thermo Nicolet spectrometer (Nexus 470, USA), equipped with an MCT–A detector, with resolution of 4 cm⁻¹ and in a high-temperature chamber (SpectraTech) with ZnSe windows. The outlet line of the chamber was coupled to a Pfeiffer mass spectrometer; model QMS Prisma (Aßlar, Germany), equipped with the CH-TRON detector. The catalyst was pre-treated in situ under H_2 flow (40 mL/min) from room temperature to 300 °C, at heating rate of 5 °C/min for 1 h. Then, the sample was cooled down to 150°C. AcOH was saturated for 1 h, to stabilize the AcOH concentration. Afterwards, the O_2 flow (20 mL/min, 5 vol% in He) and the C_2H_4 flow (10 mL/min) were adjusted. Reagents were mixed in the mass flow controller passing through the saturator. Spectra were taken using the reduced sample as background and stored as averages of 150 scans. The reaction was carried out for 1 h at each temperature (150, 180, 200°C) and the spectra were obtained after 10 minutes of reaction. Then, the surface was cleaned with helium to remove AcOH, C_2H_4 and O_2, and analyzed. Finally, the temperature was adjusted for the next condition.

Conflict of Interest

The authors declare no conflict of interest.

[1] A. W. Budiman, J. S. Nam, J. H. Park, R. I. Mukti, T. S. Chang, J. W. Bae, M. J. Choi, *Catal. Surv. Asia* **2016**, *20*, 173–193.
[2] F. W. Speetjens, M. K. Mahanthappa, *Macromolecules* **2015**, *48*, 5412–5422.
[3] N. Ben Halima, *RSC Adv.* **2016**, *6*, 39823–39832.
[4] M. Chen, D. Kumar, C.-W. Yi, D. W. Goodman, *Science.* **2015**, *310*, 291–300.
[5] M. S. Chen, K. Luo, T. Wei, Z. Yan, D. kumar, C. W. Yi, D. W. Goodman, *Catal. Today.* **2006**, *117*, 37–45.
[6] D. Yuan, X. Gong, R. Wu, *J. Phys. Chem. C* **2008**, *112*, 1539–1543.
[7] M. García-Mota, N. López, *J. Am. Chem. Soc.* **2008**, *130*, 14406–14407.
[8] F. Gao, D. W. Goodman, *Chem. Soc. Rev.* **2012**, *41*, 8009–8020.
[9] E. K. Hanrieder, A. Jentys, J. A. Lercher, *J. Catal.* **2016**, *333*, 71–77.
[10] E. K. Hanrieder, A. Jentys, J. A. Lercher, *ACS Catal.* **2015**, *5*, 5776–5786.
[11] M. B. Gawande, A. Goswami, F. X. Felpin, T. Asefa, X. X. Huang, R. Silva, X. X. Zou, R. Zboril, S. Varma, *Chem. Rev.* **2016**, *116*, 3722–3811.
[12] D. J. Stacchiola, *Acc. Chem. Res.* **2015**, *48*, 2151–2158.
[13] K. V. R. Chary, G. V. Sagar, C. S. Srikanth, V. V. Rao, *J. Phys. Chem. B* **2007**, *111*, 543–550.
[14] Y. Zhu, Y. Zhu, G. Ding, S. Zhu, H. Zheng, Y. Li, *Appl. Catal. A* **2013**, *468*, 296–304.
[15] H. Zhang, Z. Wang, S. Li, Y. Jiao, J. Wang, Q. Zhu, X. Li, *Appl. Therm. Eng.* **2017**, *111*, 811–818.
[16] E. Hernández-Ramirez, J. A. Wang, L. F. Chen, M. A. Valenzuela, A. K. Dalai, *Appl. Surf. Sci.* **2017**, *399*, 77–85.
[17] J. Gu, Y.-W. Zhang, F. (Feng) Tao, *Chem. Soc. Rev.* **2012**, 8050–8065.
[18] G. Zhao, F. Yang, Z. Chen, Q. Liu, Y. Ji, Y. Zhang, Z. Niu, J. Mao, X. Bao, P. Hu, Y. Li, *Nat. Commun.* **2017**, *8*, 14039.
[19] J. H. Bang, K. S. Suslick, *Adv. Mater.* **2010**, *22*, 1039–1059.
[20] Y. Xu, L. Chen, X. Wang, W. Yao, Q. Zhang, *Nanoscale* **2015**, *7*, 10559–10583.
[21] G. Roscher, *Ullmann's Ency. Ind. Chem., Vol. 38.* Wiley-VCH Verlag GmbH & Co. KGaA, **2000**. pp 107–123.
[22] D. D. Kragten, R. A. van Santen, M. K. Crawford, W. D. Provine, J. J. Lerou, *Inorg. Chem.* **1999**, *38*, 331–339.
[23] M. Sankar, N. Dimitratos, P. J. Miedziak, P. P. Wells, C. J. Kiely, G. J. Hutchings, *Chem. Soc. Rev.* **2012**, 8099–8139.
[24] X. Li, X. Wang, M. Liu, H. Liu, Q. Chen, Y. Yin, M. Jin, *Nano Res.* **2018**, *11*, 780–790.
[25] H. Li, X. Zhao, H. Liu, S. Chen, X. Yang, C. Lv, H. Zhang, X. She, D. Yang, *Small* **2018**, *14*, 1802824.
[26] M. D. Marcinkowski, A. D. Jewell, M. Stamatakis, M. B. Boucher, E. A. Lewis, C. J. Murphy, G. Kyriakou, E. C. H. Sykes, *Nat. Mater.* **2013**, *12*, 523–528.
[27] G. X. Pei, X. Y. Liu, X. Yang, L. Zhang, A. Wang, L. Li, H. Wang, X. Wang, T. Zhang, *ACS Cat.* **2017**, *7*, 1491–1500.
[28] Y. Liu, Y. He, D. Zhou, J. Feng, D. Li, *Catal. Sci. Technol.* **2016**, *6*, 3027–3037.
[29] Axel, G, *J. Phys. Condens. Matter* **2009**, *21*, 084205.
[30] X. Cao, A. Mirjalili, J. Wheeler, W. Xie, B. W. L. Jang, *Front. Chem. Sci. Eng.* **2015**, *9*, 442–449.
[31] Z. Xu, L. Chen, Y. Shao, D. Yin, S. Zheng, *Ind. Eng. Chem. Res.* **2009**, *48*, 8356–8363.
[32] X. Cao, Y. Ji, Y. Luo, *J. Phys. Chem. C* **2015**, *119*, 1016–1023.
[33] S. Shan, V. Petkov, B. Prasai, J. Wu, P. Joseph, Z. Skeete, E. Kim, D. Mott, O. Malis, J. Luo, *Nanoscale* **2015**, *7*, 18936–18948.
[34] K. A. Goulas, S. Sreekumar, Y. Song, P. Kharidehal, G. Gunbas, P. J. Dietrich, G. R. Johnson, Y. C. Wang, A. M. Grippo, L. C. Grabow, *J. Am. Chem. Soc.* **2016**, *138*, 6805–6812.
[35] F. Cai, L. Yang, S. Shan, D. Mott, B. Chen, J. Luo, C.-J. Zhong, *Catalysts* **2016**, *6*, 96.
[36] J. Gu, Y. W. Zhang, F. Tao, *Chem. Soc. Rev.* **2012**, *41*, 8050–8065.
[37] F. R. Lucci, J. Liu, M. D. Marcinkowski, M. Yang, L. F. Allard, M. Flytzani-Stephanopoulos, E. C. H. Sykes, *Nat. Commun.* **2015**, *6*.
[38] A. R. González, Y. J. O. Asencios, E. M. Assaf, J. M. Assaf, *Appl. Surf. Sci.* **2013**, *280*, 876–877.
[39] F. M. Anzures, F. C. Rivas, J. H. Ventura, P. S. Hernández, G. Berlier, G. Zacahua-Tlacuatl, *Appl. Catal. A* **2015**, *489*, 218–225.
[40] P. Estifaee, M. Haghighi, N. Mohammadi, F. Rahmani, *Ultrason. Sonochem.* **2014**, *21*, 1155–1165.

[41] G. Suresh, J. Radnik, V. N. Kalevaru, M.-M. Pohl, M. Schneider, B. Lucke, A. Martin, N. Madaan, A. Bruckner, *Phys. Chem. Chem. Phys.* **2010**, *12*, 4833–4842.

[42] V. V Srdić, S. Rakić, Ž. Cvejić, *Mater. Res. Bull.* **2008**, *43*, 2727–2735.

[43] U. Troitzsch, *J. Am. Ceram. Soc.* **2006**, *89*, 3201–3210.

[44] F. Frusteri, L. Frusteri, F. Costa, A. Mezzapica, C. Cannilla, G. Bonura, *Appl. Catal. A* **2017**, *545*, 24–32.

[45] S. Gatla, N. Madaan, J. Radnik, V. N. Kalevaru, M.-M. Pohl, B. Lücke, A. Martin, A. Brückner, *Appl. Catal. A* **2011**, *398*, 104–112.

[46] J. S. Valente, M. S. Cantú, J. G. H. Cortez, R. Montiel, X. Bokhimi, E. López-Salinas, *J. Phys. Chem. C.* **2007**, *111*, 642–651.

[47] Q. Zhao, J. Wang, X. Huang, Y. Yao, W. Zhang, L. Shao, *Electrochem. Commun.* **2016**, *69*, 55–58.

[48] G. Águila, F. Gracia, P. Araya , *Appl. Catal. A* **2008**, *343*, 16–24

[49] X. Jiang, N. Koizumi, X. Guo, C. Song, *Appl. Catal. B.* **2015**, 170–171.

[50] T. Klimova, M. L. Rojas, P. Castillo, R. Cuevas, J. Ramírez, *Microporous Mesoporous Mater.* **1998**, *20*, 293–306.

[51] P. R. Coffman, C. K. Barlingay, A. Gupta, S. K. Dey, *J. Sol-Gel Sci. Technol.* **1996**, *6*, 83–106.

[52] A. K. Bhattacharya, K. K. Mallick, A. Hartridge, J. L. Woodhead, *J. Mater. Sci.* **1996**, *31*, 267–271.

[53] M. Kikugawa, K. Yamazaki, H. Shinjoh, *Appl. Catal. A* **2017**, *547*, 199–204.

[54] K. V. R. Chary, G. V. Sagar, D. Naresh, K. K. Seela, B. Sridhar, *J. Phys. Chem. B* **2005**, *109*, 9437–9444.

[55] P. Mierczynski, R. Ciesielski, A. Kedziora, W. Maniukiewicz, T. P. Maniecki, *Catalysis in Industry* **2017**, *9*, 99–103.

[56] J. Batista, A. Pintar, D. Mandrino, M. Jenko, V. Martin, *Appl. Catal. A Gen.* **2001**, *206*, 113–124.

[57] H. Y. T. Chen, J. P. Chou, C. Y. Lin, C. W. Hu, Y. T. Yang, T. Y. Chen, *Nanoscale* **2017**, *9*, 7207–7216.

[58] R. Basnayake, Z. Li, S. Katar, W. Zhou, H. Rivera, E. S. Smotkin, D. J. Casadonte, C. Korzeniewski, *Langmuir* **2006**, *22*, 10446–10450.

[59] Y. F. Han, D. Kumar, C. Sivadinarayana, D. W. Goodman, *J. Catal.* **2004**, *224*, 60–68.

[60] Z. Wei, R. Pan, Y. Hou, Y. Yang, Y. Liu, *Sci. Rep.* **2015**, *5*.

[61] Z. Yin, D. Gao, S. Yao, B. Zhao, F. Cai, L. Lin, P. Tang, P. Zhai, G. Wang, D. Ma, *Nano Energy* **2016**, *27*, 35–43.

[62] J. L. Davis, M. A. Barteau, *Surf. Sci.* **1991**, *256*, 50–66.

[63] P. P. Du, X. C. Hu, X. Wang, C. Ma, M. Du, J. Zeng, C. J. Jia, Y. Y. Huang, R. Si, *Inorg. Chem. Front.* **2017**, *4*, 668–674.

[64] H. L. Tierney, A. E. Baber, J. R. Kitchin, E. C. H. Sykes, *Phys. Rev. Lett.* **2009**, *103*.

[65] P. Concepción, M. Boronat, S. García-García, E. Fernández, A. Corma, *ACS Catal.* **2017**, *7*, 3560–3568.

[66] Y. Huang, X. Dong, Y. Yu, M. Zhang, *Appl. Surf. Sci.* **2016**, *387*, 1021–1028.

[67] Y. Huang, X. Dong, Y. Yu, *Catal. Lett.* **2016**, *146*, 2516–2533.

[68] D. Stacchiola, F. Calaza, L. Burkholder, W. T. Tysoe, *J. Am. Chem. Soc.* **2004**, *126*, 15384–15385.

[69] M. Kuhn, J. Jeschke, S. Schulze, M. Hietschold, H. Lang, T. Schwarz, *Catal. Commun.* **2014**, *57*, 78–82.

[70] B. Samanos, P. Boutry, R. Montarnal, *J. Catal.* **1971**, *23*, 19–30.

[71] M. CHEN, D. W. GOODMAN, *Chin. J. Catal.* **2008**, *29*, 1178–1186.

[72] W. Wang, F. Yuan, X. Niu, Y. Zhu, *Sci. Rep.* **2016**, *6*, 19511

[73] G. K. Reddy, C. Ling, T. C. Peck, H. Jia, *RSC Adv.* **2017**, *7*, 19645–19655.

[74] W. Cai, R. Mu, S. Zha, G. Sun, S. Chen, Z. Zhao, *Sci. Adv.* **2018**, 1–9.

[75] J. Song, X. Wang, J. Yan, J. Yu, G. Sun, B. Ding, *Sci. Rep.* **2017**, *7*, 1636.

[76] S. M. Augustine, J. P. Blitz, *J. Catal.* **1993**, *142*, 312–324.

[77] S. Kouva, K. Honkala, L. Lefferts, J. Kanervo, *Catal. Sci. Technol.* **2015**, *5*, 3473–3490.

[78] D. Stacchiola, F. Calaza, L. Burkholder, A. W. Schwabacher, M. Neurock, W. T. Tysoe, *Angew. Chem. Int. Ed.* **2005**, *44*, 4572–4574; *Angew. Chem.* **2005**, *117*, 4648–4650.

[79] H. Olcay, L. Xu, Y. Xu, G. W. Huber, *ChemCatChem* **2010**, *2*, 1420–1424.

[80] Y. Zhu, Y. Zhu, X. Kong, D. B. Cao, J. Cui, Y. W. Li, *ACS Catal.* **2014**, *4*, 3675–3681.

[81] K. Mallikarjuna, H. Kim, *Colloids Surf. A.* **2017**, *535*, 194–200.